

# Enhancement of Retinal Fundus Images via Pixel Color Amplification

Alex Gaudio<sup>1[0000-0003-1380-6620]</sup>, Asim Smailagic<sup>1[0000-0001-8524-997X]</sup>, and Aurélio Campilho<sup>2,3[0000-0002-5317-6275]</sup>

<sup>1</sup> Carnegie Mellon University, Pittsburgh PA 15213, USA

<sup>2</sup> INESC TEC, Porto

<sup>3</sup> Faculty of Engineering, University of Porto

`agaudio@andrew.cmu.edu, asim@cs.cmu.edu, campilho@fe.up.pt`

**Abstract.** Obscured by muted presentation, troves of colorful detail lie within retinal fundus images. Interpretation of these images is essential to diagnostic Ophthalmology, where detection of certain fine details directly relates to a prognosis. We propose a pixel color amplification theory and family of enhancement methods to facilitate detection and segmentation tasks on retinal images. Our novel re-interpretation of the image distortion model underlying dehazing theory shows how three existing priors commonly used by the dehazing community and a novel fourth prior are related. We utilize the theory to develop a family of enhancement methods for retinal images, including novel methods for whole image brightening and darkening as well as image sharpening and a derivation of the Unsharp Masking algorithm. We evaluate the enhancement methods both independently of an image processing model, and in conjunction as a pre-processing step. Our results show large increases in deep network performance on three grading, five lesion segmentation and four vessel segmentation tasks from three corresponding retinal image datasets. Relative to our no-enhancement baseline, we improve Matthew’s Correlation Coefficient by as much as 0.22 on grading tasks, and Dice score increases by 0.491 and 0.209 on lesion and vessel segmentation tasks. We provide evidence that our enhancement preprocessing is useful for unbalanced and difficult datasets, we show that the enhancements can perform class balancing by composing them together, and also demonstrate that the methods indeed separate important features by color.

**Keywords:** Image Enhancement · Medical Image Analysis · Dehazing · Segmentation

## 1 Introduction

Image enhancement is a process of removing noise from images in order to improve performance on a future image processing task. We consider image-to-image pre-processing methods intended to facilitate a downstream image processing task such as Diabetic Retinopathy lesion segmentation, where the goal is to identify which pixels in an image of a human retina are pathological. In this setting, image

enhancement does not in itself perform segmentation, but rather it elucidates relevant features. Fig. 1 shows an example enhancement with our method, which transforms the color of individual pixels and enhances fine detail.

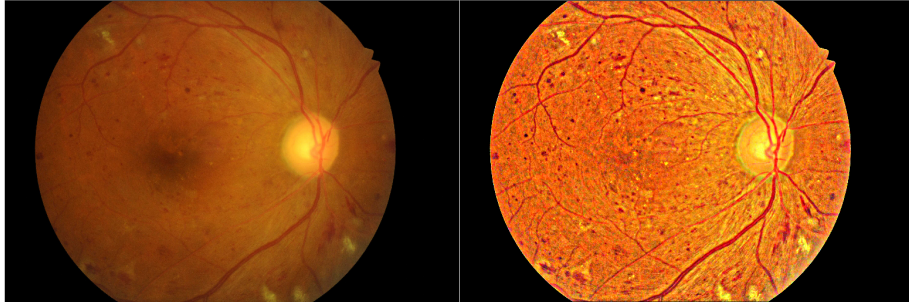


Fig. 1: Comparing unmodified image (left) to our enhancement of it (right).

Our main contributions are to re-interpret the distortion model underlying dehazing theory as a theory of pixel color amplification. Building on the widely known Dark Channel Prior method [6], we show a novel relationship between three previously known priors and a fourth novel prior. We then use these four priors to develop a family of brightening and darkening methods. Next, we show how the theory can derive the Unsharp Masking method for image sharpening. Finally, we apply these theoretical results to the domain of retinal fundus images. We develop a separability measure to guide development of the pre-processing models, and then we show how the pre-processing enhancement methods significantly improve performance of deep convolutional networks on five lesion segmentation tasks, four vessel segmentation tasks, and three grading tasks. We also open source our code as the Image Enhancement Toolkit for Retinal Fundus Images (IETK-Ret) [3].

Section 2 presents a known interpretation of dehazing theory as way to describe image distortion. Section 3 re-interprets the theory as pixel color amplification. Section 4 presents our experiments on retinal fundus images and associated evaluation strategies. Section 5 shows that our methods improve performance by a large margin on all tasks and sheds insight into the variety of ways the enhancements are useful.

## 2 Related Work

Natural images are distorted by refraction of light as it travels through the transmission medium (such as air), causing modified pixel intensities in the color channels of the image. A widely used physical theory for this distortion has traditionally been used for single image dehazing [1,6,10,19]:

$$\mathbf{I}(\mathbf{x}) = \mathbf{J}(\mathbf{x})t(\mathbf{x}) + \mathbf{A}(1 - t(\mathbf{x})), \quad (1)$$

where each pixel location,  $\mathbf{x}$ , in the distorted RGB image,  $\mathbf{I}$ , can be constructed as a function of the distortion-free radiance image  $\mathbf{J}$ , a grayscale transmission map image  $\mathbf{t}$  quantifying the relative portion of the light ray coming from the observed surface in  $\mathbf{I}(\mathbf{x})$  that was not scattered (and where  $t(\mathbf{x}) \in [0, 1] \forall \mathbf{x}$ ), and an atmosphere term,  $\mathbf{A}$ , which is typically a RGB vector that approximates the color of the uniform scattering of light. Since scattering of light conserves energy, the distortion is an attenuation of the signal is replaced by the color of the surrounding atmosphere  $\mathbf{A}$ . Indeed, distortion is simply a non-negative airlight term  $\mathbf{A}(1 - t(\mathbf{x}))$ . We refer to [1] for a deeper treatment of the physics behind the theory in a dehazing context. Obtaining a distortion free image  $\mathbf{J}$  via this theory is typically a three step process. Given  $\mathbf{I}$ , define an atmosphere term  $\mathbf{A}$ , solve for the transmission map  $\mathbf{t}$ , and then solve for  $\mathbf{J}$ . We develop new insights into this theory by demonstrating ways in which it can behave as a pixel amplifier when  $\mathbf{t}$  and  $\mathbf{A}$  are allowed to be three channel images.

The well known Dark Channel Prior (DCP) method [6,9] addresses the dehazing task for Eq. (1) by imposing a prior assumption on RGB images. The assumption differentiates the noisy (hazy) image,  $\mathbf{I}$ , from its noise free (dehazed) image,  $\mathbf{J}$ . That is, in any haze-free multi-channel region of a RGB image, at least one pixel has zero intensity in at least one channel ( $\{(0, g, b), (r, 0, b), (r, g, 0)\}$ ), while a hazy region will have no pixels with zero intensity ( $r > 0, g > 0, b > 0$ ). The assumption is invalid when any channel of a given region is sparse. To quantify distortion in an image, the assumption justifies creating a fourth channel, known as the dark channel, by applying a min operator convolutionally to each region of the images  $\mathbf{I}$  and  $\mathbf{J}$ . Specifically,  $\tilde{\mathbf{I}}^{\text{dark}}(\mathbf{x}) = \min_c \min_{\mathbf{y} \in \Omega_{\mathbf{I}}(\mathbf{x})} \frac{I^{(c)}(\mathbf{y})}{A^c}$ , where  $c$  denotes the color channel (red, green or blue) and  $\Omega_{\mathbf{I}}(\mathbf{x})$  is a set of pixels in  $\mathbf{I}$  neighboring pixel  $\mathbf{x}$ . The min operator causes  $\tilde{\mathbf{I}}^{\text{dark}}$  to lose fine detail, but an edge-preserving filter known as the guided filter [7] restores detail  $\mathbf{I}^{\text{dark}} = g(\tilde{\mathbf{I}}^{\text{dark}}, \mathbf{I})$ . While  $\mathbf{J}^{\text{dark}}(\mathbf{x})$  always equals zero and therefore cancels out of the equations,  $\mathbf{I}^{\text{dark}}(\mathbf{x})$  is non-zero in hazy regions. By observing that the distortion free image  $\mathbf{J}^{\text{dark}}$  is entirely zero while  $\mathbf{I}^{\text{dark}}$  is not entirely zero, solving Eq. (1) for  $\mathbf{t}$  leads to Eq. (4) and then Eq. (5) in Fig. 2. In practice, the denominator of (5) is  $\max(t(\mathbf{x}), \epsilon)$  to avoid numerical instability or division by zero; this amounts to preserving a small amount of distortion in heavily distorted pixels. Fig. 2 summarizes the mathematics.

The DCP method permits various kinds of inversions. The bright channel prior [21] solves for a transmission map by swapping the min operator for a max operator in Eq. (4). This prior was shown useful for exposure correction. Fig. 2 shows our variation of the bright channel prior based more directly on DCP mathematics and with an incorporated guided filter. Another simple modification of the DCP method is to invert the input image  $\mathbf{I}$ . Using this approach, it was recently shown that the distortion theory in Eq. (1) and associated dehazing methods can perform illumination correction [15,2,16]. The central idea is to invert the image, apply the dehazing equations, and then invert the dehazed result. We demonstrate the mathematics of this inverted DCP method in Figure 2. Color illumination literature requires the assumption that  $\mathbf{A} = (1, 1, 1)$ , meaning

|  |     | Inverted DCP (Illumination<br>Correction)  |      |
|--|-----|--|------|
| <b>Dark Channel Prior (Dehazing)</b>   |     |  |      |
| $\mathbf{A} = (r, g, b).$  | (2) | $\mathbf{A} = (1, 1, 1).$  | (7)  |
| $\tilde{t}(\mathbf{x}) = 1 - \min_c \min_{\mathbf{y} \in \Omega_I(\mathbf{x})} \frac{I^c(\mathbf{y})}{A^c}$        | (3) | $\mathbf{J} = 1 - f_{DCP}(1 - \mathbf{I}, \mathbf{A})$   | (8)  |
| $t(\mathbf{x}) = \text{guidedFilter}(\mathbf{I}, \tilde{t}(\mathbf{x})).$  | (4) | <b>Bright Channel Prior (Exposure<br/>Correction)</b>  |      |
| $\mathbf{J}(\mathbf{x}) = \frac{\mathbf{I}(\mathbf{x}) - \mathbf{A}}{\max(t(\mathbf{x}), \epsilon)} + \mathbf{A}.$ | (5) | $\tilde{t}(x) = 1 - \max_c \max_{\mathbf{y} \in \Omega_I(\mathbf{x})} \frac{I^c(\mathbf{y})}{A^c}$ | (9)  |
| $\implies \mathbf{J} = f_{DCP}(\mathbf{I}, \mathbf{A})$  | (6) | $t(\mathbf{x}) = \text{guidedFilter}(\mathbf{I}, \tilde{t}(\mathbf{x})).$                          | (10) |
|  |     | $\implies \mathbf{J} = f_{BCP}(\mathbf{I}, \mathbf{A})$  | (11) |

Fig. 2: **Left:** Dark Channel Prior (DCP) method for dehazing. Given an (inverted) image  $\mathbf{I}$  and atmosphere  $\mathbf{A}$ , obtain transmission map  $\mathbf{t}$  and then recover  $\mathbf{J}$ , the undistorted image. **Top and Bottom Right:** Two priors based on inversion of the Dark Channel Prior.

the image is white-balanced. In the dehazing context, this assumption would mean the distorted pixels are too bright, but in the color illumination context, distorted pixels are too dark. In the Methods section, we expand on the concept of brightness and darkness as pixel color amplification, show the theory supports other values of  $\mathbf{A}$ , and we also expand on the concept of inversion of Eqs. (4) and (5) for a wider variety of image enhancements.

### 3 Methods

The distortion theory Eq. (1) is useful for image enhancement. In section 3.1, we show how the theory is a pixel color amplifier. In section 3.2, we show ways in which the theory is invertible. We apply these properties to derive a novel prior and present a unified view of amplification under four distinct priors. Sections 3.2 and 3.2 apply the amplification theory to three specific enhancement methods: whole image brightening, whole image darkening and sharpening.

#### 3.1 The distortion theory amplifies pixel intensities

We assume that  $\mathbf{A}$ ,  $\mathbf{I}$  and  $\mathbf{J}$  share the same space of pixel intensities, so that in any given channel  $c$  and pixel location  $\mathbf{x}$ , the intensities  $A^c$ ,  $I^c(\mathbf{x})$  and  $J^c(\mathbf{x})$  can all have the same maximum or minimum value. We can derive the simple equation  $t(\mathbf{x}) = \frac{I^{(c)}(\mathbf{x}) - A^{(c)}}{J^{(c)}(\mathbf{x}) - A^{(c)}} \in [0, 1]$  from Eq. (1) by noting that the distortion theory presents a linear system containing three channels. The range of  $\mathbf{t}$  implies the numerator and denominator must have the same sign. For example, if  $A^{(c)} \geq$

$I^{(c)}(\mathbf{x})$ , then the numerator and denominator are non-positive and  $J^{(c)}(\mathbf{x}) \leq I^{(c)}(\mathbf{x}) \leq A^{(c)}$ . Likewise, when  $A^{(c)} \leq I^{(c)}(\mathbf{x})$ , the order is reversed  $J^{(c)}(\mathbf{x}) \geq I^{(c)}(\mathbf{x}) \geq A^{(c)}$ . These two ordering properties show the distortion theory amplifies pixel intensities. The key insight is that the choice of  $\mathbf{A}$  determines how the color of each pixel in the recovered image  $\mathbf{J}$  changes. Models that recover  $\mathbf{J}$  using Eq. (1) will simply amplify color values for each pixel  $\mathbf{x}$  in the direction  $\mathbf{I}(\mathbf{x}) - \mathbf{A}$ .

**Atmosphere controls the direction of amplification in color space.** The atmosphere term  $\mathbf{A}$  is traditionally a single RGB color vector with three scalar values,  $A = (r, g, b)$ , but it can also be an RGB image matrix. As a RGB vector,  $\mathbf{A}$  does not provide precise pixel level control over the amplification direction. For instance, two pixels with the same intensity are guaranteed to change color in the same direction, even though it may be desirable for these pixels to change color in opposite directions. Fortunately, considering  $\mathbf{A}$  as a three channel RGB image enables precise pixel level control of the amplification direction. It is physically valid to consider  $\mathbf{A}$  as an image since the atmospheric light may shift color across the image, for instance due to a change in light source. As an image,  $\mathbf{A}$  can be chosen to define the direction of color amplification  $I^c(\mathbf{x}) - A^c(\mathbf{x})$  for each pixel and each color channel independently.

**Transmission map and Atmosphere both control the rate of amplification.** Both the transmission map  $\mathbf{t}$  and the magnitude of the atmosphere term  $\mathbf{A}$  determine the amount or rate of pixel color amplification. The effect on amplification is shown in the equation  $\mathbf{J} = \frac{\mathbf{I}-\mathbf{A}}{\mathbf{t}} + \mathbf{A}$ , where the difference  $\mathbf{I} - \mathbf{A}$  controls the direction and magnitude of amplification and  $\mathbf{t}$  affects the amount of difference to amplify. The transmission map itself is typically a grayscale image matrix, but it can also be a scalar constant or a three channel color image. Each value  $t(\mathbf{x}) \in [0, 1]$  is a mixing coefficient specifying what proportion of the signal is not distorted. When  $t(\mathbf{x}) = 1$ , there is no distortion; the distorted pixel  $\mathbf{I}(\mathbf{x})$  and corresponding undistorted pixel  $\mathbf{J}(\mathbf{x})$  are the same since  $\mathbf{I}(\mathbf{x}) = \mathbf{J}(\mathbf{x})1 + 0$ . As  $t(\mathbf{x})$  approaches zero, the distortion caused by the difference between the distorted image  $\mathbf{I}$  and the atmosphere increases.

### 3.2 Amplification under inversion

The distortion theory supports several kinds of inversion. The equations (4) and (5) are invertible. The input image  $\mathbf{I}$  can also undergo invertible transformations. We prove these inversion properties and show why they are useful.

**Inverting Eq. (4) results in a novel DCP-based prior.** We discussed in Related Work three distinct priors that provide a transmission map: the traditional DCP approach with Eq. (4); the bright channel prior in Eq. (10); and color illumination via Eq. (8). Bright channel prior and color illumination respectively perform two types of inversion; the former changes the min operator to a max operator while the latter inverts the image  $1 - \mathbf{I}$ . Combining these two inversion techniques results in a novel fourth prior. In Table 1, we show the four transmission maps. We show that each prior has a solution using either the min or max operator, which is apparent by the following two identities:

Table 1: Four transmission maps derived from variations of Eq. (4). For clear notation, we used the vectorized functions  $\mathbf{t} = \text{solveMin\_t}(\mathbf{I}, \mathbf{A}) = 1 - \min_c \min_{\mathbf{y} \in \Omega_{I(\mathbf{x})}} \frac{I^c(\mathbf{y})}{A^c}$  and  $\mathbf{t} = \text{solveMax\_t}(\mathbf{I}, \mathbf{A}) = 1 - \max_c \max_{\mathbf{y} \in \Omega_{I(\mathbf{x})}} \frac{I^c(\mathbf{y})}{A^c}$ .

|                      | Amplify Dark Areas   | Amplify Bright Areas  |
|----------------------|--|---|
| Weak Amplification   | $\text{solveMin\_t}(1 - \mathbf{I}, \mathbf{A} = 1)$<br>$1 - \text{solveMax\_t}(\mathbf{I}, \mathbf{A} = 1)$<br>Color Illumination Prior | $\text{solveMin\_t}(\mathbf{I}, \mathbf{A} = 1)$<br>$1 - \text{solveMax\_t}(1 - \mathbf{I}, \mathbf{A} = 1)$<br>Standard Dark Channel Prior |
|                      | $1 - \text{solveMin\_t}(\mathbf{I}, \mathbf{A} = 1)$<br>$\text{solveMax\_t}(1 - \mathbf{I}, \mathbf{A} = 1)$                             | $1 - \text{solveMin\_t}(1 - \mathbf{I}, \mathbf{A} = 1)$<br>$\text{solveMax\_t}(\mathbf{I}, \mathbf{A} = 1)$                                |
|                      | Our novel prior  | Bright Channel Prior  |
| Strong Amplification |  |   |

$$\text{solve\_t}(\mathbf{I}, \mathbf{A}) = 1 - \min_c \min_{\mathbf{y} \in \Omega_{I(\mathbf{x})}} \frac{I^c(\mathbf{y})}{A^c} \equiv \max_c \max_{\mathbf{y} \in \Omega_{I(\mathbf{x})}} \frac{1 - I^c(\mathbf{y})}{A^c} \quad (12)$$

$$\text{solve\_t}(\mathbf{I}, \mathbf{A}) = 1 - \max_c \max_{\mathbf{y} \in \Omega_{I(\mathbf{x})}} \frac{I^c(\mathbf{y})}{A^c} \equiv \min_c \min_{\mathbf{y} \in \Omega_{I(\mathbf{x})}} \frac{1 - I^c(\mathbf{y})}{A^c} \quad (13)$$

The unified view of these four priors in Table 1 provides a novel insight into how they are related. In particular, the table provides proof that the Color Illumination Prior and Bright Channel Prior are inversely equivalent. Similarly, DCP and our prior are also inversely equivalent. It distinguishes between weak and strong amplification, and amplification of bright and dark pixel neighborhoods.

In Appendix A, we visualize these four transmission maps to demonstrate how they collectively perform strong or weak amplification of bright or dark regions of the input image. In this paper, we set  $\mathbf{A} = \mathbf{1}$  when solving for  $\mathbf{t}$ . Any choice of  $\mathbf{A}^c \in (0, 1]$  is valid, and when all  $\mathbf{A}^c$  are equal, smaller values of  $\mathbf{A}$  are guaranteed to amplify the differences between these properties further.

**Inverting Eq. (5) motivates brightening and darkening.** Given an image  $\mathbf{I}$ , transmission map  $\mathbf{t}$  and an atmosphere  $\mathbf{A}$ , solving for the recovered image  $\mathbf{J}$  with Eq. (5) can be computed two equivalent ways, as we demonstrate by the following identity:

$$\mathbf{J} = \text{solve\_J}(\mathbf{I}, \mathbf{t}, \mathbf{A}) \equiv 1 - \text{solve\_J}(1 - \mathbf{I}, \mathbf{t}, 1 - \mathbf{A}) \quad (14)$$

The proof is by simplification of  $\frac{1 - \mathbf{A}}{\mathbf{t}} + \mathbf{A} = 1 - \left( \frac{(1 - \mathbf{I}) - (1 - \mathbf{A})}{\mathbf{t}} + (1 - \mathbf{A}) \right)$ . It implies the space of possible atmospheric light values, which is bounded in  $[0, 1]$ , is symmetric under inversion.

We next prove that solving for  $\mathbf{J}$  via the color illumination method [15, 2, 16] is equivalent to direct attenuation  $\mathbf{J} = \frac{\mathbf{I}}{\mathbf{t}}$ , a fact that was not clear in prior work. As we noted in Eq. (8), color illumination solves  $\mathbf{J} = 1 - \frac{(1 - \mathbf{I}) - \mathbf{A}}{\mathbf{t}} + \mathbf{A}$  under the required assumption that  $\mathbf{A} = \mathbf{1}$ . We can also write the atmosphere as  $\mathbf{A} = 1 - \mathbf{0}$ . Then, the right hand side of (14) leads to  $\mathbf{J} = 1 - \text{solve\_J}(1 - \mathbf{I}, \mathbf{t}, \mathbf{A} = 1 - \mathbf{0}) =$

$\frac{\mathbf{I}-\mathbf{0}}{t} + \mathbf{0}$ . Therefore, color illumination actually performs whole image brightening with the atmosphere  $\mathbf{A} = (0, 0, 0)$  even though the transmission map uses a white-balanced image assumption that  $\mathbf{A} = (1, 1, 1)$ . Both this proof and the invertibility property Eq. (14) motivate Section 3.2 where we perform brightening and darkening with all priors in Table 1.

**Application to Whole Image Brightening and Darkening.** Brightening versus darkening of colors is a matter of choosing an amplification direction. Extremal choices of the atmosphere term  $\mathbf{A}$  result in brightening or darkening of all pixels in the image. For instance,  $\mathbf{A} = (1, 1, 1)$  guarantees for each pixel  $\mathbf{x}$  that the recovered color  $\mathbf{J}(\mathbf{x})$  is darker than the distorted color  $\mathbf{I}(\mathbf{x})$  since  $\mathbf{J} \leq \mathbf{I} \leq \mathbf{A}$ , while  $\mathbf{A} = (0, 0, 0)$  guarantees image brightening  $\mathbf{J} \geq \mathbf{I} \geq \mathbf{A}$ . More generally, any  $\mathbf{A}$  satisfying  $1 \geq A^c \geq \max_{\mathbf{x}} I^c(\mathbf{x})$  performs whole image brightening and any  $\mathbf{A}$  satisfying  $0 \leq A^c \leq \min_{\mathbf{x}} I^c(\mathbf{x})$  performs whole image darkening. We utilize the four distinct transmission maps from Table 1 to perform brightening  $\mathbf{A} = \mathbf{0}$  or darkening  $\mathbf{A} = \mathbf{1}$ , resulting in eight kinds of amplification. We describe and visualize these maps and corresponding brightening and darkening techniques applied to retinal fundus images in Appendix B. Our application of the Bright Channel Prior and Color Illumination Prior for whole image darkening is novel. Utilizing our prior for brightening and darkening is also novel.

**Application to Image Sharpening.** We show a novel connection between dehazing theory and *unsharp masking*, a deblurring method and standard image sharpening technique that amplifies fine detail [11]. Consider  $\mathbf{A}$  as a three channel image obtained by applying a non-linear blur operator to  $\mathbf{I}$ ,  $\mathbf{A} = \text{blurry}(\mathbf{I})$ . Solving Eq. (1) for  $\mathbf{J}$  gives  $\mathbf{J} = \frac{1}{t}\mathbf{I} - \frac{(1-t)}{t}\mathbf{A}$ . Since each scalar value  $t(\mathbf{x})$  is in  $[0, 1]$ , we can represent the fraction  $t(\mathbf{x}) = \frac{1}{u(x)}$ . Substituting, we have the simplified matrix form  $\mathbf{J} = \mathbf{u} \circ \mathbf{I} - (\mathbf{u} - 1) \circ \text{blurry}(\mathbf{I})$  where the  $\circ$  operator denotes element-wise multiplication with broadcasting across channels. This form is precisely *unsharp masking*, where  $\mathbf{u}$  is either a constant, or  $\mathbf{u}$  is a 1-channel image matrix determining how much to sharpen each pixel. The matrix form of  $\mathbf{u}$  is known as locally adaptive unsharp masking. Thus, we show the distortion theory in Eq. (1) is equivalent to image sharpening by choosing  $\mathbf{A}$  to be a blurred version of the original input image. In Appendix C, we demonstrate two sharpening algorithms applied to retinal fundus images, where one algorithm utilizes a scalar  $t$  and the second utilizes a three channel Laplacian image as  $t$ .

## 4 Experiments

In this section, we design and evaluate enhancement methods useful to segmentation and detection tasks on retinal fundus images. We first introduce three datasets: IDRiD, ARSN, and RITE. Next, we describe our evaluation methods. Third, we present pre-processing methods useful to disease grading, lesion segmentation, and blood vessel segmentation.

#### 4.1 Datasets

The **Indian Diabetic Retinopathy Dataset (IDRiD)** [14] contains 81 retinal fundus images for segmentation, with a train-test split of 54:27 images. Each image is 4288x2848 pixels. Each pixel has five binary labels for presence of: Microaneurysms (MA), Hemorrhages (HE), Hard Exudates (EX), Soft Exudates (SE) and Optic Disc (OD). Only 53:27 and 26:14 images present HE and SE, respectively. Table 3 shows the number of positive pixels per category (left columns) and within categories (right columns).

Table 2: Dataset class distributions, computed over pixels on left and number of images on right.

| Category | Table 3: IDRiD Dataset |            |               | Table 4: QualDR Dataset |       |       |       |       |      |       |      |       |      |
|----------|------------------------|------------|---------------|-------------------------|-------|-------|-------|-------|------|-------|------|-------|------|
|          | Pos                    | $\sum$ Pos | Pos/(Pos+Neg) | DR                      | MD    | PC    | Grade | Train | Test | Train | Test | Train | Test |
|          | Train                  | Test       | Train         | Test                    | Grade | Train | Test  | Train | Test | Train | Test | Train | Test |
| MA       | 0.027                  | 0.024      | 0.071         | 0.033                   | -1.0  | 54    | 30    | 227   | 101  | 73    | 37   |       |      |
| HE       | 0.253                  | 0.256      | 0.657         | 0.355                   | 0.0   | 315   | 119   | 500   | 209  | 735   | 306  |       |      |
| EX       | 0.207                  | 0.261      | 0.538         | 0.362                   | 1.0   | 158   | 63    | 102   | 46   | 11    | 4    |       |      |
| SE       | 0.049                  | 0.043      | 0.126         | 0.060                   | 2.0   | 187   | 89    | —     | —    | 10    | 9    |       |      |
| OD       | 0.464                  | 0.416      | 1.204         | 0.577                   | 3.0   | 42    | 21    | —     | —    | —     | —    |       |      |
|          |                        |            |               |                         | 4.0   | 73    | 34    | —     | —    | —     | —    |       |      |

The **Retinal Images vessel Tree Extraction (RITE)** [8] dataset contains 20 training and 20 testing images. Each image is accompanied by a binary segmentation map of the blood vessels as well as a labeled segmentation map in which the vessels are further classified as arteries or veins. The 40 images are inherited from the DRIVE database [17]. When creating ground truth, human annotators were instructed to label a pixel as vessel if at least 70% certain.

The **Quality and Diabetic Retinopathy DataBase (QualDR)** [20] is a private dataset of 1185 retinal fundus images of varying dimensions and image quality that we split into training and test sets of 829 and 356 images respectively. Each image is graded for Diabetic Retinopathy (DR), Macular Degeneration (MD), and Photocoagulation (PC) by Ophthalmologists. The DR grades are numbered from zero (healthy) to four (very diseased), MD grades are binary and PC grades are range from zero (no scar tissue) to two (extensive scar tissue). In addition, if grades are marked as ungradable, such as due to a poor quality image, we assign a negative one. DR, MD and PC class distributions are unbalanced, as shown in Table 4. Several images show disagreement between physicians, and we assign the grade that was most common among them.

## 4.2 Evaluation Methods

We evaluate our enhancement methods on the domain of retinal fundus images via two distinct strategies. First, we evaluate the methods independently of a segmentation model. We design a Separability score (4.2) to explain whether a pre-processing method separates colors in a way that facilitates segmentation. Second, we measure how the pre-processing method affects performance of a deep network on segmentation and grading tasks (4.2).

**Separability score: Are foreground and background colors separable?**  
The motivation for a separability score is two-fold:

*Explainability:* Does a preprocessing method separate colors in a way that makes the segmentation task easier? We hypothesize that a segmentation task is easier if the respective distributions of foreground and of background pixel colors are maximally separable. We propose a Separability score to quantify the separation of these distributions given an image or dataset with pixel labels.

*Guide development of preprocessing methods:* Downstream segmentation or grading models introduce bias and variance that complicate evaluation and development of a pre-processing method. For instance, a deep network requiring heavy regularization may actually perform worse from a pre-processing *enhancement* method; the network may require additional regularization before enhancement is useful. Downstream models add extra complexity and implementation challenges. Faced with such difficulties, we propose an evaluation method that is independent of downstream models. Our Separability score for retinal fundus images guides development of the proposed pre-processing methods and enables choosing useful hyperparameters that perform enhancement. We justify the score is in fact a useful development aid in our Results, Section 5.2.

We define the Separability Score on the IDRiD dataset as an aggregation of a set of Two-Sample Kolmogorov-Smirnov Tests (KS) into a single scalar, under a null hypothesis for each test that foreground and background pixel intensities are drawn from the same distribution. We compute one test per color channel and lesion type and image available in the IDRiD training dataset. For each KS test, a low KS score (close to zero) indicates the foreground and background pixels are hard to separate, while a KS score close to one indicates the healthy and diseased pixels have been enhanced. Separability is defined as:

$$S_{\text{KS}}^{c,l,\mathbf{I}} = \max_{\mathbf{x} \in \mathbf{I}} |F^{c,l}(x) - B^{c,l}(x)|, \quad \Rightarrow \quad S = \max_c \min_{l,i} S_{\text{KS}}^{c,l}(\mathbf{I}) \quad (15)$$

Where  $F^c(\mathbf{x})$  and  $B^c(\mathbf{x})$  are the cumulative distributions of foreground (healthy) and background (diseased) pixel intensities given a red, green or blue color channel  $c$  of image  $\mathbf{I}$  and a corresponding lesion mask  $l$  from the IDRiD dataset  $\mathcal{D}$  of MA, HE, SE, EX or OD pixel annotations.

**Blackbox Evaluation: Does an enhancement method improve performance?** While the separability score explains that a method *should* facilitate

segmentation, it does not empirically prove a method is actually useful to a particular model and task. This fact motivates evaluation with deep networks. We measure how introduction of a pre-processing enhancement method affects performance of deep networks on grading and segmentation tasks. We now describe the network architectures and performance measures for grading and segmentation:

**Grading Tasks on QualDR.** We define grading of a retinal fundus image as the process of diagnosing a stage of development of a pathology. We train deep models to perform three grading tasks on the QualDR dataset: DR, MD, and PC. We use the EfficientNet (b4) architecture [18] pretrained on ImageNet, with 13 output classes to simultaneously grade all three tasks. The loss function is the average of three weighted cross entropy loss functions, one per task. The weights vector for each task’s loss is  $\text{weights} = \left( \frac{\max_i w_i}{\mathbf{w}} \right)$  for a column vector  $\mathbf{w}$  defined in Table 4. The Adam Optimizer (minibatch size 8, learning rate 0.0002, weight decay 0.0001) was used. We also applied the following pre-processing: center crop the fundus to minimize background, resize to (512x512) pixels, apply the pre-processing enhancement method (independent variable), clip pixel values into [0,1], randomly rotate and flip, and apply cutout (set three random (102x102) patches of the image all zero). Cutout, rotations and flipping were only applied on the training set; we excluded them from validation and test sets. Each time we train a model, we hold out a random 20% of training images as a validation set, and we use the set to apply early stopping with a patience of 15 epochs. Finally, after each epoch we compute three confusion matrices, one per task.

To evaluate performance, we implement a multi-class generalization of Matthew’s Correlation Coefficient (MCC). MCC, also known as the phi coefficient, is the Pearson correlation of a confusion matrix and ranges from  $[-1, +1]$ . It is regarded as one of the best ways to reduce a confusion matrix to a single number and is preferable to specificity and sensitivity for unbalanced datasets [12], although it is undefined if the confusion matrix contains a zero. Our implementation follows the work of [4,5]. We compute a baseline MCC value by using an identity function as the enhancement method. We evaluate other enhancement methods by measuring relative difference in MCC from the baseline identity function.

**Lesion and Vessel Tree Segmentations on IDRiD and RITE.** We implement a segmentation model with a standard U-Net network architecture [13] and evaluate change in performance via the Dice coefficient. We apply this model to artery, vein, artery and vein overlap (also known as vessel crossings), and overall vessel segmentation tasks on the RITE dataset, and to five segmentation tasks (MA, HE, SE, EX, OD) on the IDRiD dataset. The RITE model has four output channels, while IDRiD has five. We use a binary cross entropy loss summed over all pixels and output channels. On IDRiD, we apply task balancing weights to ensure equal contribution of positive pixels to the loss. The weights are computed via  $\left( \frac{\max_i w_i}{\mathbf{w}} \right)$ , where the vector  $\mathbf{w}$  contains counts of positive pixels across all IDRiD training images for each of the 5 task categories (see left column of Table 3). Without the weighting, the model did not learn to segment MA, HE, and EX. The Adam Optimizer has a learning rate 0.001 and weight decay

0.0001. The preprocessing steps are the same as those for grading, but we did not include cutout. We randomly hold out two training images as the validation set in order to apply early stopping with a patience of 30 epochs. We evaluate the segmentation performance on the respective test sets with the Sørensen-Dice coefficient, which is commonly used for medical image segmentation.

### 4.3 Pre-Processing Enhancement Methods for Retinal Fundus Images

We combine the brightening, darkening and sharpening methods together and perform an ablation study. We assign the eight methods in Appendix B a letter. The brightening methods, from top left to bottom right are A,B,C,D. The corresponding darkening methods are W,X,Y,Z. We also apply sharpening via Algo. 2 in Appendix C. Combined methods assume the following notation:  $A + X$  is the average of of  $A$  and  $X$ , which is then sharpened;  $sA + sX$  is the average of sharpened  $A$  with sharpened  $X$ . A standalone letter  $X$  is a sharpened  $X$ . All methods have the same hyperparameters, which we found suitable for all retinal images we evaluated. When solving for  $t$ , the size of the neighborhood  $\Omega$  is (5x5); the guided filter for  $t$  has radius=100,  $\epsilon = 1e^{-8}$ . When solving for  $J$ , the max operator in the denominator is  $\max(\min(t)/2, 1e - 8)$ . For sharpening, we blur using a guided filter (radius=30,  $\epsilon = 1e^{-8}$ ) with the other hyperparameters defined in the appendix, and we do not use a guided filter to denoise as the images are previously resized to (512x512). These hyperparameters and the averaging strategy was chosen by evaluating the Separability score on a subset of IDRiD training images.

## 5 Results

### 5.1 Our pre-processing enhancement methods significantly improve performance on all tasks.

We show the model with highest test performance in each task category in Tables 6 (QualDR), 5 (IDRiD), and 7 (RITE). The pre-processing enhancement methods significantly improve performance over the baseline identity function for all grading and segmentation tasks, underscoring the value of our enhancement preprocessing theory and methods.

**Enhancement improves detection of rare classes.** QualDR grading results in Table 6 show improvements over the baseline in all three categories. PC grading improves over the baseline by a large amount (0.22). PC is a highly unbalanced class, and the MCC score, which is well suited to unbalanced datasets, increases significantly if the model can detect rare classes. IDRiD and RITE datasets are also unbalanced, and the reported improvements in their respective tables further supports this claim.

**Enhancement can be class balancing.** IDRiD results in Table 5 present significant improvements over the baseline identity model for all tasks, showing

Table 5: IDRiD: Top Models

| Task      | Method           | Dice (delta)  |
|-----------|------------------|---------------|
| <b>EX</b> | avg4:sA+sC+sX+sZ | 0.728 (0.407) |
|           | avg2:sA+sZ       | 0.615 (0.295) |
| <b>HE</b> | avg3:sA+sC+sX    | 0.491 (0.491) |
|           | avg3:sB+sC+sX    | 0.368 (0.368) |
| <b>MA</b> | avg4:A+B+C+X     | 0.251 (0.251) |
|           | avg2:sB+sX       | 0.219 (0.219) |
| <b>OD</b> | avg4:sA+sC+sX+sZ | 0.876 (0.359) |
|           | avg2:sA+sZ       | 0.860 (0.343) |
| <b>SE</b> | avg4:sA+sC+sX+sZ | 0.491 (0.332) |
|           | avg3:B+C+X       | 0.481 (0.322) |

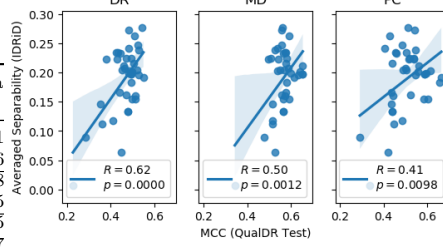
Table 6: QualDR: Top Models

| Task      | Method              | MCC (delta)   |
|-----------|---------------------|---------------|
| <b>DR</b> | avg3:A+B+X          | 0.549 (0.071) |
|           | avg2:sC+sX          | 0.544 (0.066) |
| <b>MD</b> | avg5:sA+sB+sC+sW+sX | 0.654 (0.088) |
|           | avg4:A+B+C+X        | 0.651 (0.085) |
| <b>PC</b> | avg3:A+B+X          | 0.663 (0.225) |
|           | B                   | 0.655 (0.217) |

Table 7: RITE: Top Models

| Task            | Method           | Dice (delta)  |
|-----------------|------------------|---------------|
| <b>Arteries</b> | avg4:sA+sB+sC+sX | 0.602 (0.127) |
|                 | avg2:C+X         | 0.591 (0.116) |
| <b>Overlap</b>  | avg2:sC+sX       | 0.336 (0.209) |
|                 | avg3:sA+sC+sX    | 0.334 (0.207) |
| <b>Veins</b>    | avg2:sC+sX       | 0.677 (0.083) |
|                 | avg3:A+C+X       | 0.674 (0.080) |
| <b>Vessels</b>  | avg2:sC+sX       | 0.818 (0.056) |
|                 | avg2:C+X         | 0.815 (0.054) |

Fig. 3: Performance Evaluation



improvements over the baseline between 0.251 and 0.491. Our analysis of the IDRiD results in particular support the primary hypothesis that enhancement makes the segmentation task easier. We observe in the table a juxtaposition between the segmentation of three bright features, EX, SE and OD, and two dark features, MA and HE. Notably, the delta values show the baseline identity model did not learn on dark task categories (MA, HE). Indeed, while training the models on IDRiD, we initially found that the model learned to segment only the optic disc (OD). Of the categories, OD has the most extremal intensities (brightest) and is typically the largest feature by pixel count in a fundus image; the gradients from other tasks were overshadowed by OD gradients. To address this problem, we implemented a category balancing weight. From the results, we can conclude the gradients from bright features EX, OD and SE overpower gradients from dark features MA and HE. This makes sense since bright categories outnumber dark categories three to two. This need to carefully weigh the loss function suggests differences in color intensity values *causes* differences in performance. It is therefore particularly interesting that the enhancement methods were able to learn despite also being subject to these issues. In fact, we can observe that the best enhancements in the table incorporate the Z method, which performs a strong darkening of bright regions. The RITE and QualDR datasets do not list Z at all. We interpret this result as strong evidence that our enhancement methods make the segmentation task easier, and in fact, that they can be used as a form of class balancing by image color augmentation.

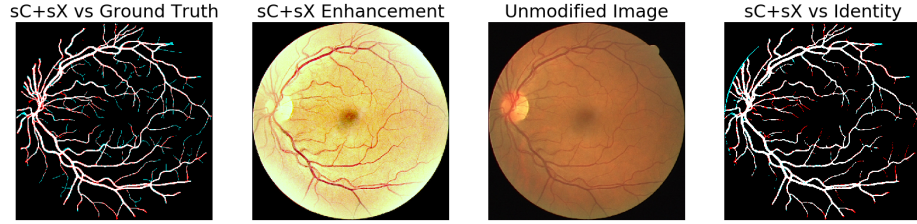


**Fig. 4: Vessel Segmentation on RITE.** White pixels show agreement. Red pixels show sC+sX model predicted positive. Cyan pixels show the ground truth (left) or baseline identity (right) predicted positive. Using our enhancement results in a better vessel tree.

**Enhancement can improve the ground truth.** RITE results in Table 7 also show strong improvements, and Fig. 4 visualizes the output of a vessel segmentation of a RITE test set image (the alphabetically first image by filename). The presence of C methods in the table coincides with visual intuition that C should be good at segmentation; C is visualized in Fig. 9 and Fig. 8. On the left in Fig. 4, we compare the sC+sX segmentation model output to the ground truth. On far right, we compare the sC+sX output to the baseline identity model output. The presence of red lines in the right-most plot shows that sC+sX enhancement improves the network’s ability to find smaller vessels. The left-most plot shows that the model still misses a few small vessels (in cyan), but small red patches that fill in gaps in the ground truth data suggest an improvement over the ground truth. Qualitatively, the enhanced image (middle left) shows the small vessels much more clearly than the unmodified image (middle right). The ground truth could be higher quality if human annotators created ground truth annotations with enhanced images.

## 5.2 Separability scores correlate with QualDR task performance

The Separability score helped us develop and tune our enhancement methods. Fig. 7 shows a positive Pearson correlation between IDRiD training set Separability and QualDR test set MCC, suggesting that a higher Separability score does coincide with better grading task performance. This is interesting since, in a purely diagnostic sense, PC and MD grading are unrelated to the lesions (MA, HE, EX and SE) that make up the Separability score. The correlation for DR grading is highest ( $R=0.62$ ,  $p < 0.00001$ ), which makes sense considering the Separability score uses the IDRiD dataset for DR segmentation. The correlation is less strong for less related tasks MD and PC, matching intuition that the features needed for grading are different, yet similar. In fact, we have some intuition for how MD and PC relate to IDRiD lesions. PC appears as bright regions (similar in color to SE or EX) sometimes with a dark spot in the center (color similar to HE). Drusen, a lesion indicative of MD, is very similar to SE and EX. The strong performance obtained by our enhancement methods and positive correlation both indicate that

the Separability score is useful to guide development of pre-processing methods independently of a downstream model because better color separation of DR lesions coincides with better grading performance.

### 5.3 Qualitative Analysis

We show results for four of the six the top performing image enhancement methods in Appendix D, excluding two methods that appeared visually redundant. In Fig. 9, each row presents a different image and each column corresponds to an enhancement method. We observe that the input images from the QualDR dataset are difficult to see and appear to have little detail, while the enhanced images are quite colorful and very detailed. The differences in bright and dark regions across each row provide intuitive sense of how averaging the individual models (Fig. 6 and 8) can affect the outcome. These images were evaluated on the QualDR dataset.

## 6 Conclusion

In this paper, we re-interpret a theory of image distortion as a pixel color amplifier and utilize the theory to develop a family of enhancement methods for retinal fundus images. We expose a previously unknown relationship between three existing priors commonly used for image dehazing with a fourth novel prior. We apply our theory to the application of whole image brightening and darkening, resulting in a eight enhancement methods, four of which are also novel (methods C, W, Y, and Z). We also show a derivation of the Unsharp Masking algorithm for image sharpening and develop a novel sharpening algorithm for retinal fundus images. Finally, we evaluate our enhancement methods on the domain of retinal fundus images. First, we create a Separability score to evaluate the enhancements independently of an image processing model. Using the enhancement methods as preprocessing methods, we show significant increases in deep network performance on three grading, five lesion segmentation and four vessel segmentation tasks from three corresponding retinal image datasets. We show the enhancement methods are useful for unbalanced and difficult datasets and show that they can perform class balancing. We suggest using enhancements in development of new datasets to improve ground truth labels. Our pixel color amplification theory applied to retinal fundus images yields a variety of rich and colorful enhancements, as shown by our compositions of methods A-D and W-Z, and the theory shows great promise for wider adoption by the community.

## Acknowledgements

We thank Dr. Alexander R. Gaudio, a retinal specialist and expert in degenerative retinal diseases, for his positive feedback and education of fundus images.

Supported in part by the National Funds through the Fundação para a Ciência e a Tecnologia within under Project CMUPERI/TIC/0028/2014.

## 7 Appendix

### A Relationship and Properties of Four Priors, Visualized on Retinal Images

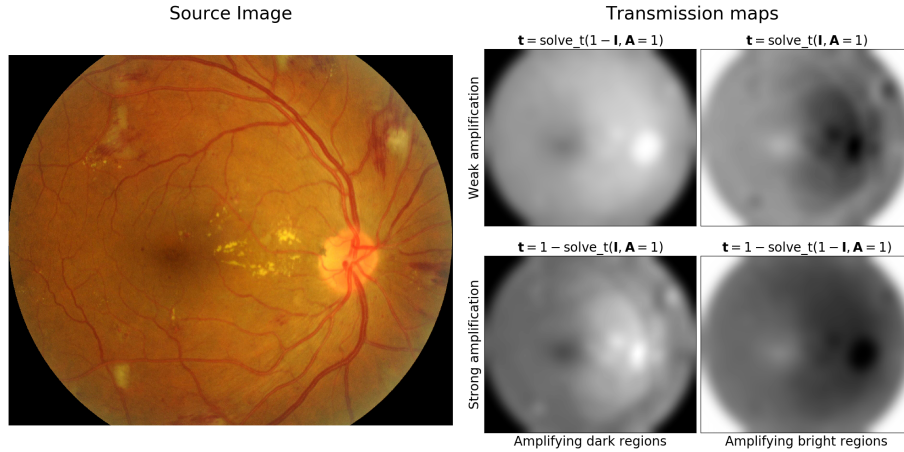


Fig. 5: The transmission maps (right) obtained from source image (left) selectively amplify bright or dark regions. The darkest pixels of the transmission map correspond to a larger amount of amplification. To generate the figure, we randomly sample a retinal fundus image from the IDRiD dataset (dataset described in Section 4.1). We ignore the blue channel when computing the transmission map for the top right and bottom left maps because the min values of the blue channel in retinal fundus images are noisy.

We describe and visualize four transmission maps presented in Table 1. The transmission map  $\mathbf{t}$  determines how much to amplify each pixel, where values of  $t(\mathbf{x})$  close to zero result in stronger amplification than values close to one. Recalling Eq. (4), we define the vectorized function over all pixels  $\mathbf{x}$  as  $\mathbf{t} = \text{solve\_t}(\mathbf{I}, \mathbf{A}) = \text{guidedFilter}(1 - \min_c \min_{y \in \Omega_{I(\mathbf{x})}} \frac{I^c(y)}{A^c}, \mathbf{I})$ . Simple variations on this equation lead to different kinds of amplification, as shown in Fig. 5. In the figure, the top left and bottom right transmission maps are inversely equivalent and are derived from the image's minimum pixel intensity values. The top right and bottom left are also inversely equivalent, and they are derived from the image's maximum pixel intensity values. We have found the resulting transmission map is sensitive to the chosen neighborhood size  $\Omega$ .

## B Whole Image Amplification via DCP

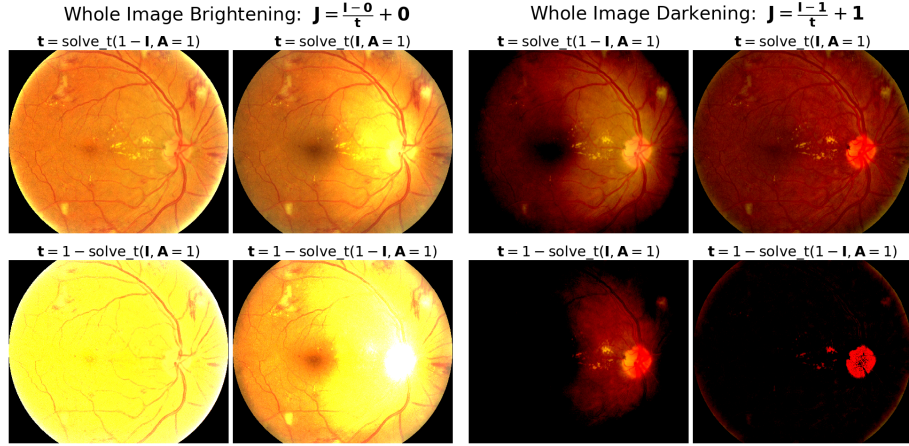


Fig. 6: Whole image Brightening (Left) and Darkening (Right) using the corresponding four transmission maps in Fig. 5. Note that when solving for the transmission map,  $\mathbf{A} = \mathbf{1}$  in all cases, but when performing brightening or darkening,  $\mathbf{A}$  is  $\mathbf{0}$  or  $\mathbf{1}$  respectively. For visualization, the images are clipped to  $[0, 1]$ , but the methods generate color values that may be outside of the  $[0, 1]$  range.

We visualize whole image brightening  $\mathbf{A} = \mathbf{0}$  or whole image darkening  $\mathbf{A} = \mathbf{1}$  with  $t$  corresponding to the four transmission maps shown in Appendix A.

## C Sharpening Retinal Fundus Images

We present two sharpening algorithms, Algo. 1 and 2, and show their respective outputs in Fig. 7. Sharpening amplifies differences between an image and a blurry version of itself. In unevenly illuminated images, the dark or bright regions may saturate. Therefore, the use of a scalar transmission map (middle image, Algo. 1) implies that the input image should ideally have even illumination. The optional guided filter in the last step provides edge preserving smoothing and helps to minimize speckle noise, but can cause too much blurring on small images.

Algo. 1, the simplest sharpening method, can over-sharpen noisy regions. Algo. 2 improves on it by selectively amplifying only the regions that have an edge. Edges are found by deriving a three channel transmission map from a Laplacian filter applied to a morphologically smoothed fundus image. We enhance edges by recursively sharpening the Laplace transmission map under the theory. Fig. 8 shows the results of composing each of the brightening or darkening methods in Fig. 6 with Algo. 2.

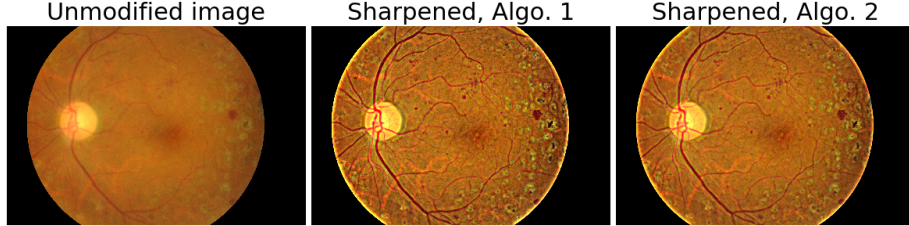


Fig. 7: Sharpening a retinal fundus image with Algo. 1. Image is randomly sampled from the IDRiD training dataset (described in Sec. 4.1).

| <b>Algorithm 1:</b> Image Sharpening, simple   | <b>Algorithm 2:</b> Image Sharpening, complex   |
|--|---|
| <b>Input:</b> $\mathbf{I}$ (input fundus image)<br><b>Result:</b> $\mathbf{J}$ (sharpened image)<br>$\mathbf{A} = \text{blur}(\mathbf{I}, \text{blur\_radius});$<br>$t = 0.15;$<br><b>if</b> $\min(\text{img\_width}, \text{img\_height}) > 1500$ <b>then</b><br>  $\mathbf{J} = \text{guidedFilter}(\text{guide} = \mathbf{I} - \mathbf{A}, \text{src} = \frac{\mathbf{I} - \mathbf{A}}{t} + \mathbf{A});$<br><b>else</b><br>  $\mathbf{J} = \frac{\mathbf{I} - \mathbf{A}}{t} + \mathbf{A};$<br><b>end</b> | <b>Input:</b> $\mathbf{I}$ (input fundus image)<br><b>Result:</b> $\mathbf{J}$ (sharpened image)<br>$\tilde{\mathbf{t}} = \text{Algo\_1}(\mathbf{I}, \text{morphological\_laplace}(\mathbf{I}, (2, 2, 1)));$<br>$\tilde{\mathbf{t}} = 1 - \frac{\tilde{\mathbf{t}} - \min(\tilde{\mathbf{t}})}{\max(\tilde{\mathbf{t}}) - \min(\tilde{\mathbf{t}})};$<br>$\mathbf{t} = \text{elementwise\_max}(10^{-8}, \text{elementwise\_max}(\tilde{\mathbf{t}}, \frac{\min(\tilde{\mathbf{t}})}{2}));$<br>$\mathbf{J} = \text{Algo\_1}(\mathbf{I}, \mathbf{t} = \mathbf{t});$ |

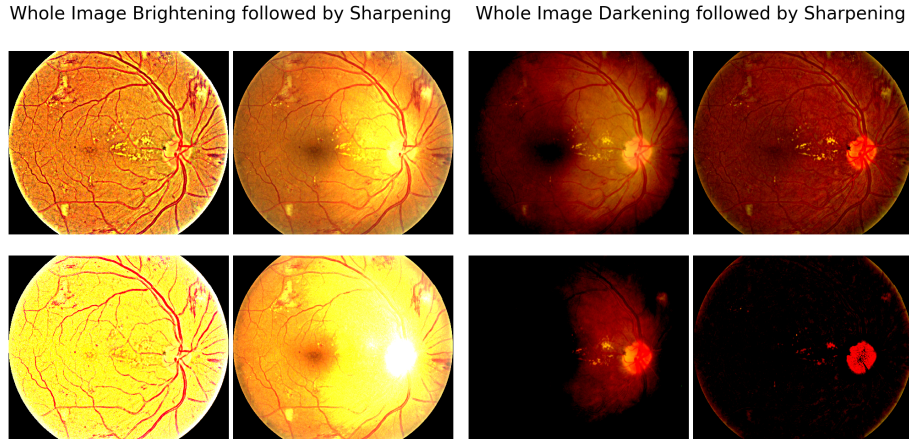


Fig. 8: The result of sharpening each image in Fig. 6 using Algo. 2.

## D Qualitative Results on the QualDR dataset

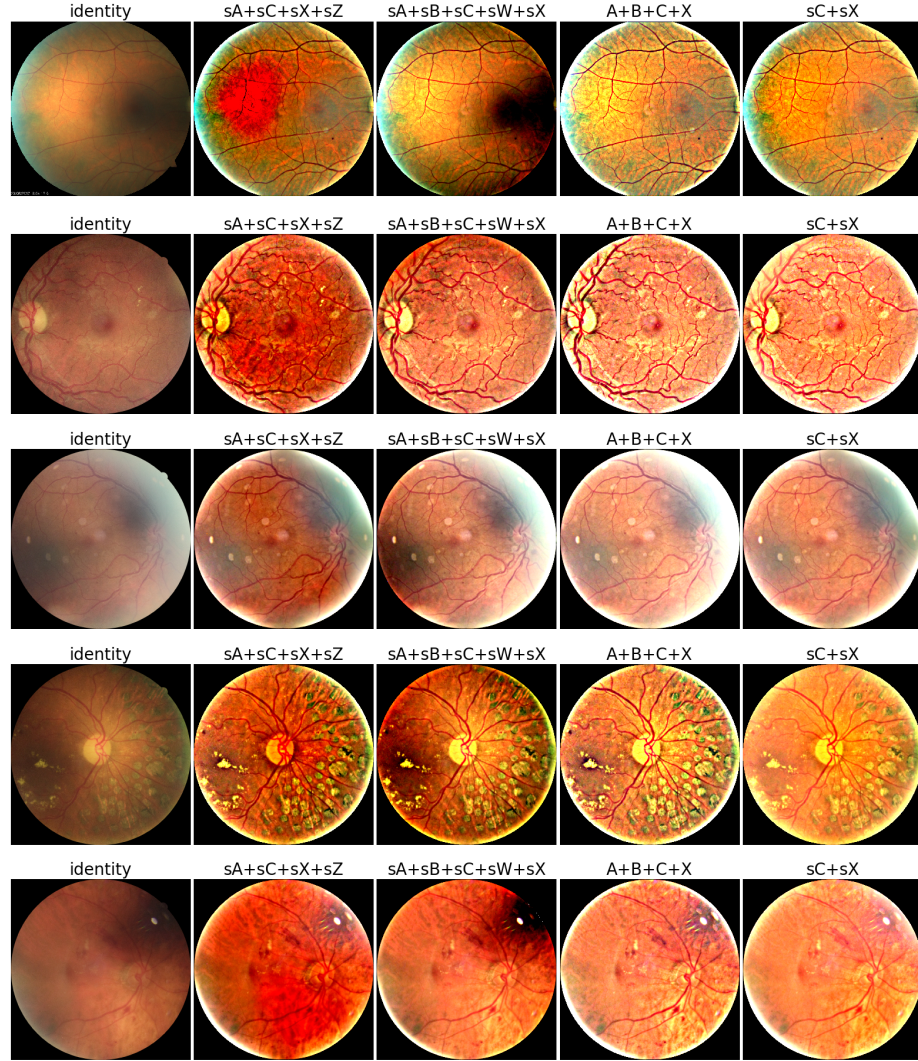


Fig. 9: Visualization of our enhancement methods. Each row is an image. Each column is an enhancement method.

## References

1. Fattal, R.: Single image dehazing. ACM Trans. Graph. **27**(3), 72:1–72:9 (Aug 2008). <https://doi.org/10.1145/1360612.1360671>, <http://doi.acm.org/10.1145/1360612.1360671>

- 1360612.1360671
2. Galdran, A., Bria, A., Alvarez-Gila, A., Vazquez-Corral, J., Bertalmio, M.: On the duality between retinex and image dehazing. 2018 IEEE/CVF Conference on Computer Vision and Pattern Recognition (Jun 2018). <https://doi.org/10.1109/cvpr.2018.00857>, <http://dx.doi.org/10.1109/cvpr.2018.00857>
  3. Gaudio, A.: Pixel color amplification with ietk-ret. <https://github.com/adgaudio/ietk-ret> (2020)
  4. Gorodkin, J.: Comparing two k-category assignments by a k-category correlation coefficient. Computational Biology and Chemistry **28**(5), 367 – 374 (2004). <https://doi.org/https://doi.org/10.1016/j.combiolchem.2004.09.006>, <http://www.sciencedirect.com/science/article/pii/S1476927104000799>
  5. Gorodkin, J.: The rk page (2006), <http://rk.kvl.dk/software/rkorrC>
  6. He, K., Sun, J., Tang, X.: Single image haze removal using dark channel prior. IEEE Transactions on Pattern Analysis and Machine Intelligence **33**(12), 2341–2353 (Dec 2011). <https://doi.org/10.1109/TPAMI.2010.168>
  7. He, K., Sun, J., Tang, X.: Guided image filtering. IEEE Transactions on Pattern Analysis and Machine Intelligence **35**(6), 1397–1409 (June 2013). <https://doi.org/10.1109/TPAMI.2012.213>
  8. Hu, Q., Abràmoff, M.D., Garvin, M.K.: Automated separation of binary overlapping trees in low-contrast color retinal images. In: Mori, K., Sakuma, I., Sato, Y., Barillot, C., Navab, N. (eds.) Medical Image Computing and Computer-Assisted Intervention – MICCAI 2013. pp. 436–443. Springer Berlin Heidelberg, Berlin, Heidelberg (2013)
  9. Lee, S., Yun, S., Nam, J.H., Won, C.S., Jung, S.W.: A review on dark channel prior based image dehazing algorithms. EURASIP Journal on Image and Video Processing **2016**(1), 4 (Jan 2016). <https://doi.org/10.1186/s13640-016-0104-y>, <https://doi.org/10.1186/s13640-016-0104-y>
  10. Narasimhan, S.G., Nayar, S.K.: Vision and the atmosphere. IJCV **48**(3), 233–254 (January 2002)
  11. Petrou, M., Petrou, C.: Image Processing: The Fundamentals, pp. 357–360. John Wiley & Sons, Ltd, Chichester, UK (2011-01-27)
  12. Powers, D.: Evaluation: From precision, recall and f-measure to roc, informedness, markedness & correlation. J. Mach. Learn. Technol **2**, 2229–3981 (01 2011). <https://doi.org/10.9735/2229-3981>
  13. Ronneberger, O., Fischer, P., Brox, T.: U-net: Convolutional networks for biomedical image segmentation. In: Navab, N., Hornegger, J., Wells, W.M., Frangi, A.F. (eds.) Medical Image Computing and Computer-Assisted Intervention – MICCAI 2015. pp. 234–241. Springer International Publishing, Cham (2015)
  14. Sahasrabuddhe, P.P.S.P.R.K.M.K.G.D.V., Meriaudeau, F.: Indian diabetic retinopathy image dataset (idrid) (2018). <https://doi.org/10.21227/H25W98>, <http://dx.doi.org/10.21227/H25W98>
  15. Savelli, B., Bria, A., Galdran, A., Marrocco, C., Molinara, M., Campilho, A., Tortorella, F.: Illumination correction by dehazing for retinal vessel segmentation. In: 2017 IEEE 30th International Symposium on Computer-Based Medical Systems (CBMS). pp. 219–224 (June 2017). <https://doi.org/10.1109/CBMS.2017.28>
  16. Smailagic, A., Sharan, A., Costa, P., Galdran, A., Gaudio, A., Campilho, A.: Learned pre-processing for automatic diabetic retinopathy detection on eye fundus images. In: Karray, F., Campilho, A., Yu, A. (eds.) Image Analysis and Recognition. pp. 362–368. Springer International Publishing, Cham (2019)

17. Staal, J., Abramoff, M.D., Niemeijer, M., Viergever, M.A., van Ginneken, B.: Ridge-based vessel segmentation in color images of the retina. *IEEE Transactions on Medical Imaging* **23**(4), 501–509 (April 2004). <https://doi.org/10.1109/TMI.2004.825627>
18. Tan, M., Le, Q.: EfficientNet: Rethinking model scaling for convolutional neural networks. In: Chaudhuri, K., Salakhutdinov, R. (eds.) *Proceedings of the 36th International Conference on Machine Learning. Proceedings of Machine Learning Research*, vol. 97, pp. 6105–6114. PMLR, Long Beach, California, USA (09–15 Jun 2019), <http://proceedings.mlr.press/v97/tan19a.html>
19. Tan, R.T.: Visibility in bad weather from a single image. In: 2008 IEEE Conference on Computer Vision and Pattern Recognition. pp. 1–8 (June 2008). <https://doi.org/10.1109/CVPR.2008.4587643>
20. Wanderley, D.S., Araújo, T., Carvalho, C.B., Maia, C., Penas, S., Carneiro, A., Mendonça, A.M., Campilho, A.: Analysis of the performance of specialists and an automatic algorithm in retinal image quality assessment. In: 2019 IEEE 6th Portuguese Meeting on Bioengineering (ENBENG). pp. 1–4 (Feb 2019). <https://doi.org/10.1109/ENBENG.2019.8692506>
21. Wang, Y., Zhuo, S., Tao, D., Bu, J., Li, N.: Automatic local exposure correction using bright channel prior for under-exposed images. *Signal Processing* **93**(11), 3227 – 3238 (2013). <https://doi.org/https://doi.org/10.1016/j.sigpro.2013.04.025>, <http://www.sciencedirect.com/science/article/pii/S0165168413001680>